JGR Oceans

RESEARCH ARTICLE
10.1029/2022JC018723

A Nonlinear Cause for the Seasonal Predictability Barrier of SST Anomaly in the Tropical Pacific

Dakuan Yu[1], Meng Zhou[1], Chaoxun Hang[1], and De-Zheng Sun[2]

[1]School of Oceanography, Shanghai Jiao Tong University, Shanghai, China, [2]Institute of Atmospheric Sciences, Fudan University, Shanghai, China

Key Points:

- Sample Entropy method is utilized to study the nonlinearity of the seasonal Predictability Barrier (PB) of Sea Surface Temperature Anomaly (SSTA) in the tropical Pacific
- The low-amplitude background SSTA signal, which is more chaotic than the El Niño/Southern Oscillation-related signal, potentially results in PB
- The seasonal connection between SSTA and atmospheric forcing could lead to the spatial-temporal variation of the chaotic signal

Supporting Information:

Supporting Information may be found in the online version of this article.

Correspondence to:

M. Zhou,
meng.zhou@sjtu.edu.cn

Citation:

Yu, D., Zhou, M., Hang, C., & Sun, D.-Z. (2022). A nonlinear cause for the seasonal predictability barrier of SST anomaly in the tropical Pacific. *Journal of Geophysical Research: Oceans*, *127*, e2022JC018723. https://doi.org/10.1029/2022JC018723

Received 6 APR 2022
Accepted 12 OCT 2022

Author Contributions:

Conceptualization: Dakuan Yu, Meng Zhou, Chaoxun Hang, De-Zheng Sun
Data curation: Dakuan Yu
Formal analysis: Dakuan Yu, Chaoxun Hang, De-Zheng Sun
Funding acquisition: Meng Zhou
Investigation: Dakuan Yu
Methodology: Dakuan Yu
Project Administration: Meng Zhou
Resources: Dakuan Yu
Software: Dakuan Yu
Supervision: Meng Zhou
Validation: Dakuan Yu

Abstract The seasonal Predictability Barrier (PB) of Sea Surface Temperature Anomaly (SSTA) is characterized by a rapid loss of prediction skills at a particular season in dynamic models. Here, the connection between seasonal PB and the inherent nonlinearity of SSTA was investigated using a statistical method known as Sample Entropy (SamEn). When the SamEn value is large, the chaotic degree of SSTA is high. In the Niño 3 and Niño 3.4 regions, the chaotic degree of SSTA was high in the spring; in the Niño 4 region, it was high in the summer. This result was consistent with the known PB occurrence season in these regions. The month when the chaotic degree of SSTA peaked moved westward longitudinally from March to June. This spatial-temporal variation of the chaotic degree was consistent with that of the low SSTA variance and PB occurrence timing. Specifically, when the variance of SSTA was low, the low-amplitude background SSTA signal was more dominant than the El Niño/Southern Oscillation (ENSO)-related signal, the chaotic degree of SSTA was high, and the PB phenomenon occurred. Hence, the results indicated that the background SSTA signal was more chaotic than the ENSO-related signal and the seasonal PB may result from the inherent low predictability of the chaotic background SSTA signal. Furthermore, the correlation coefficient between SSTA and shortwave flux anomaly showed similar variation along the longitude compared with the chaotic degree, which suggested that the seasonal connection between SSTA and atmospheric forcing may be responsible for the spatial-temporal variation of the chaotic degree.

Plain Language Summary Accurate predictions of Sea Surface Temperature Anomaly (SSTA) in the tropical Pacific are in high demand. However, dynamic models tend to lose their prediction skills of SSTA during a certain season, which is known as the seasonal Predictability Barrier (PB). Based on a nonlinear statistic method—SamEn, the chaotic degree of SSTA was investigated in the tropical Pacific to explore the nonlinear cause for the seasonal PB. The spatial-temporal distribution of the chaotic degree was consistent with that of the PB occurrence timing and low-amplitude background SSTA signal. Specifically, when the low-amplitude background SSTA signal was dominant in SSTA data, the chaotic degree of SSTA was high, and the PB phenomenon occurred. Hence, this result suggests that the low-amplitude background SSTA signal is chaotic and the seasonal PB results from the inherent low predictability of this chaotic background SSTA signal. Furthermore, the seasonal connection between SSTA and atmospheric forcing may be responsible for the spatial-temporal variation of the chaotic degree.

1. Introduction

The Sea Surface Temperature Anomalies (SSTA) in the tropical Pacific play significant roles in affecting the global climate (Castro et al., 2001; Fereday et al., 2008; Marzban & Schaefer, 2001; McKinnon et al., 2016; H. Wang & Ting, 2000). For instance, the interannual variability of SSTA in the tropical Pacific, namely, the El Niño/Southern Oscillation (ENSO) phenomenon, not only strongly affects the climate (e.g., temperature, wind speed, precipitation, etc.) in East Asia (Gao et al., 2006; Wu et al., 2003; Yuan & Yang, 2012), and North America (Q. Hu & Feng, 2012; Infanti & Kirtman, 2016; Ropelewski & Halpert, 1986), but also has a significant impact on the variabilities of sea ice extent and concentration in the Antarctic and Arctic regions (Clancy et al., 2021; Dash et al., 2013; X. Yuan, 2004). Therefore, accurate predictions of SSTA in the tropical Pacific are crucial for decision-making as well as mitigating the risks of extreme weather (Patt & Gwata, 2002; Pierce W., 2002; Solow et al., 1998; Trenberth et al., 1998). In recent years, the 6-month advance predictions of SSTA have been achieved in the tropical Pacific through ocean-atmosphere coupled models (Song et al., 2020; Tang et al., 2018; Xue et al., 2013). However, 1-year prediction in advance is still challenging due to the so-called seasonal Predictability Barrier (PB) (Jin et al., 2008; Tang et al., 2018; van Oldenborgh et al., 2005; Webster, 1995; Webster &

Visualization: Dakuan Yu, Meng Zhou, Chaoxun Hang, De-Zheng Sun
Writing – original draft: Dakuan Yu
Writing – review & editing: Meng Zhou, Chaoxun Hang, De-Zheng Sun

Yang, 1992), which is known as a rapid loss of prediction skills in most SSTA forecast models during certain seasons (Torrence, 1998).

The PB of SSTA has been reported globally during various seasons. For example, it can be found in spring in the eastern tropical Pacific (Duan & Wei, 2013), summer in the northern Pacific Ocean and central tropical Pacific (Duan & Wu, 2015; Hou et al., 2019), and winter in the Indian Ocean Dipole region (Liu et al., 2018). Even though enormous efforts have been dedicated to investigating the features of the PB of SSTA, there is still a need for a better understanding of the mechanisms that cause the PB (Chong-Yin & Jian, 2009; Hu et al., 2014; McPhaden, 2003). Some researchers connected the PB phenomenon with some traditional statistical characteristics of observed SSTA (Ren et al., 2016; Webster & Yang., 1992). For example, Xue et al. (1994) indicated that the variance, signal-to-noise ratio, and auto correlation of monthly SSTA data in the eastern tropical Pacific are lowest in spring, and attributed the spring PB of SSTA in models to these statistic characteristics of the SSTA. However, Jin et al. (2022) suggested that the low persistence of SSTA does not always imply the low predictability of SSTA in the models, which makes the connection between these traditional statistic characteristics of SSTA data and the PB of SSTA unclear. Some researchers suggested that the PB of SSTA was triggered by the stochastic noise in the ocean and atmosphere (Lopez & Kirtman, 2014; Mukhin et al., 2021). Torrence and Webster (1998) indicated that the signal-to-noise ratio of the SSTA in the eastern tropical Pacific is lowest in spring and the air-sea coupled system is more susceptible to perturbation from the outside of the tropical dynamic system. Levine and McPhaden (2015) found that the spring PB of SSTA was more realistic compared with the observed PB in other complex models when the noise forcing is included in a conceptual recharge oscillator model. Others found that the initial errors of SSTA in the dynamic models grew rapidly in certain seasons without stochastic noises, and eventually led to the PB of SSTA (Hou et al., 2019; Larson & Kirtman, 2015; Lau & Yang, 1996; Moore, 1999). For instance, using the Zebiak-Cane dynamic model, Samelson and Tziperman (2001) revealed that the initial errors increased significantly in the growth phase of El Niño, and eventually led to the PB of SSTA in the tropical Pacific. Zheng and Zhu (2010) found that the largest initial errors occur in the spring and can strongly affect the prediction skill of SSTA in an ENSO dynamic prediction model. Hou et al. (2019) demonstrated that the initial error has the fastest growth rate in the spring of the eastern Pacific ENSO and the summer of the central Pacific ENSO based on multiple CMIP5 experiments.

There are two potential causes for the error growth of models in certain seasons (Webster, 1995; Webster & Yang, 1992). One is the missing of some key physical processes from the real world in the models (Collins et al., 2002), which means that the PB can be overcome by having a better knowledge of the air-sea coupled processes. The other is the chaotic nature of the system (Lorenz, 1963), which means that the small initial errors will grow exponentially in the models. The latter suggests that the PB is an inherent phenomenon regardless of more observations or a more accurate initial field for the models, as the exact initial information of ocean and atmosphere cannot be gained. Although the chaotic nature of the coupled system has been identified as a possible cause for the PB of SSTA in the tropical Pacific (Samelson & Tziperman, 2001), their results are based on the numerical model and cannot eliminate the effect of the deficiencies in the model. Previous studies have suggested that SSTA variability in the tropical Pacific fundamentally results from the nonlinearity of the coupled air-sea coupled system (Hua et al., 2019; Liang et al., 2012, 2017; Sun, 1997), but they did not further study the nonlinear cause for the PB of SSTA. Hence, the inherent chaotic characteristic in the coupled system as a cause for the PB phenomenon remains to be established, which is important because this nonlinear cause is closely related to the inherent prediction capability of the air-sea coupled system.

Recent progresses in time series analysis of the nonlinear systems have raised the possibility to deal with chaotic nature by extracting nonlinear dynamical information of studied systems only through analyzing observed time series (Bradley & Kantz, 2015; Fraedrich, 1987; Kantz & Schreiber, 2003; Karamperidou et al., 2014; Li & Ding, 2013). Representatives of the chaotic degree are the correlation dimension (Thelier, 1987), Lyapunov Exponents (Wolf et al., 1985), Kolmogorov Sinai Entropy (Latora & Baranger, 1999), and so on. However, the statistical methods to extract these representatives from the observed time series are applicable to infinite noiseless time series from the well-defined theoretical dynamic system, but will generate serious biases when dealing with noisy and limited-time series observed from the nonlinear systems in nature (Pincus, 1991, 1995), such as the ocean and atmosphere. Based on the information theory, a Sample Entropy (SamEn) method was proposed to quantify the chaotic degree of short and noisy time series from a nonlinear system (Richman & Moorman, 2000). When comparing the SamEn values between two different nonlinear systems, a system is more chaotic when its SamEn value is higher, and vice versa. The SamEn method is robust with noises and does not change easily

when utilizing different parameters in the calculation process (Yentes et al., 2013). The applicability of SamEn to quantify the chaotic degree and complexity of a nonlinear system has been well examined in broad disciplines including physiological time-series analysis (Eduardo Virgilio Silva & Otavio Murta, 2012; Lake et al., 2002; Richman & Moorman, 2000), de-noising for hydrologic signals (Wang et al., 2014; Zhang et al., 2019), turbulent experimental data analysis (Kim, 2021), and even the stock markets study (Shi & Shang, 2013). In this study, the SamEn method was implied to investigate the spatial-temporal distributions and variations of chaotic degrees within the air-sea coupled nonlinear system in the tropical Pacific and the connections of SamEn values with the seasonal PB of SSTA.

2. Data and Method

2.1. Data

Observed daily SSTA data from 1982 to 2021 are obtained from the NOAA Optimum Interpolation Sea Surface Temperature (OISST) V2 High-Resolution Data Set (https://psl.noaa.gov/data/gridded/data.noaa.oisst.v2.high-res.html). The OISST data set incorporates observations from different platforms (satellites, ships, buoys, and Argo floats) into a regular global grid, and has been widely used in climate assessments and monitoring (Huang et al., 2021). The longitude and latitude resolution of the data set is 0.25° between 0.125°E−359.875°E and 89.875°S−89.875°S. The data set contains the data from September 1981 to the present. In this study, the tropical Pacific is defined between 10°S and 10°N in latitude and 155°E and 90°W in longitude. The time range of observed SSTA data is from 1982 to 2021. To reduce the computational cost, the horizontal grids of OISST are interpolated to the same 2° longitude and 2° latitude grids. The finer grid than the 2° longitude and 2° latitude will not affect our results. The longitude and latitude resolution of the climatology data are 2° between 155°E−90°W and 10°S−10°N. The daily SST anomaly data are computed by removing the climatological mean daily cycle and trend from the data at each grid point. The OISST data are mainly used in Section 3.1 and Section 3.2.

The monthly ocean temperature data with the vertical profile are obtained from the HYCOM Global Ocean Forecasting System (GOFS) 3.1 reanalysis data sets (https://www.hycom.org/dataserver/gofs-3pt1/reanalysis), which have been validated against observations with consistent outcomes reported (Chassignet et al., 2007). The longitude resolution of the data set is 0.08° between 0°E and 360°E. The latitude resolution is 0.08° between 40°S−40°N and 0.04° between 40°N−90°N and 90°S−40°S. The number of vertical levels is 40. In the upper 12 m, there are seven layers, and the vertical interval is about 2 m. Between 15−50, 50–100, and 150–400 m, there are 8, 6, and 6 layers with the vertical interval of 5, 10, and 50 m, respectively. The thermocline depth is defined as the depth of 20°C isotherms in the ocean subsurface based on the HYCOM data set. The data set contains the data between 1994 and 2015, which is the maximum time range of this HYCOM GOFS 3.1 data set. The monthly net surface heat flux data are from the National Centers for Environmental Prediction (NCEP) Climate Forecast System Reanalysis (CFSR) and Climate Forecast System Version 2 (CFSv2) data, which are the surface forcing of HYCOM GOFS 3.1 reanalysis data sets. The CFSR and CFSv2 are available in the National Center for Atmospheric Research (NCAR) research data archive (https://rda.ucar.edu/). The longitude resolution of CFSR and CFSv2 data sets is 1° between 0°E and 359°E. The latitude resolution is 1° between 90°S and 90°N. The CFSR and CFSv2 data sets contain the data between 1979 and 2021. The horizontal grids of HYCOM, CFSR, and CFSv2 data sets are interpolated to the same 2° longitude and 2° latitude grids compared with the OISST data set. The monthly anomaly data are computed by removing the climatology data from the original data. The HYCOM, CFSR, and CFSv2 reanalysis data sets are mainly used in Section 3.4.

The SSTA forecast data in dynamic models are from the North American Multi-Model Ensemble (NMME) data set (http://iridl.ldeo.columbia.edu/SOURCES/.Models/.NMME/), which is the state-of-the-art coupled ensemble model to predict the SSTA variation in the tropical Pacific. It provides monthly forecast data with a maximum range between 1980 and 2021 (Kirtman et al., 2014). The NMME data set has been continuously evaluated and shows good performance of region climate predictability (Barnston et al., 2019; Becker et al., 2020). The NMME model set contains 29 different models, but only seven of them cover our study period, which is between 1982 and 2021. Therefore, in this study, the forecast data from these seven different dynamic models in the NMME model set were chosen to calculate the forecast error of SSTA in the tropical Pacific. The details of these seven different dynamic models can be found in Table 1. The SSTA forecast data are interpolated into the same 2° longitude and 2° latitude grids as the OISST observed data. Forecast errors are defined as the difference between the forecast SSTA value and the observed OISST SSTA value. The NMME forecast data set is mainly used in Section 3.3.

Table 1
The NMME Model Set Used in This Study

Model name	No. ensemble members	Hindcast period	Reference
CanCM4i	10	1981–2021	Lin et al. (2020)
CanSIPSv2	20	1981–2021	Lin et al. (2020)
COLA-RSMAS-CCSM4	10	1982–2021	Kirtman & Min (2009)
GFDL-CM2p5-FLOR-A06	12	1980–2021	Kirtman et al. (2014)
GFDL-CM2p5-FLOR-B01	12	1980–2021	Kirtman et al. (2014)
GFDL-CM2p1-aer04	10	1982–2021	Kirtman et al. (2014)
GEM-NEMO	10	1981–2021	Lin et al. (2020)

2.2. Calculation Process of the SamEn Method

The SamEn method quantifies the self-similarity degree of a time series by examining the number of instances, that two subsequences in the time series are still similar when the length of subsequences increases. More details can be found in Delgado-Bonal and Marshak (2019).

For arbitrary time-series data $H = \{H_1, H_2, H_3 \ldots H_n\}$ of length N, the time series can be reconstructed to a matrix of sequence vectors:

$$\Psi^m = \begin{bmatrix} H_1 & H_2 & \ldots & H_m \\ H_2 & H_3 & \ldots & H_{m+1} \\ \ldots & \ldots & \ldots & \ldots \\ H_{N-m} & H_{N-m+1} & \ldots & H_{N-1} \end{bmatrix} \tag{1}$$

which contains m columns and $N - m$ rows. m is the embedding dimension number (Richman & Moorman, 2000), which is the minimum time scale in this study. The length of the time series N should be larger than 200 to make the SamEn values stable (Aktaruzzaman & Sassi, 2014; Mayer et al., 2014).

The sequence vector Ψ_i^m is defined as a row in Ψ^m, which can be written as follows:

$$\Psi_i^m = \{H_i, H_{i+1} \ldots H_{i+m-1}\}\ 1 \le i \le N - m \tag{2}$$

The distance between two sequence vectors is defined as the Chebychev distance (Kløve, 2011), which is the absolute value of the elements between these two sequence vectors:

$$\mathrm{Dis}\left[\Psi_i^m, \Psi_j^m\right] = \max_{k=1,2,\ldots m} |H_{i+k} - H_{j+k}|$$
$$1 \le i, j \le N - m, i \ne j \tag{3}$$

The results would not be strongly affected by utilizing other distance types to calculate the SamEn values, such as Euclidean distance ($\mathrm{Dis}\left[\Psi_i^m, \Psi_j^m\right] = \sqrt{(H_{i+1} - H_{j+1})^2 + (H_{i+2} - H_{j+2})^2 + \ldots + (H_{i+m} - H_{j+m})^2}$), Manhattan distance ($\mathrm{Dis}\left[\Psi_i^m, \Psi_j^m\right] = \sum_{k=1}^{m} |H_{i+k} - H_{j+k}|$) (the results are not shown), as these distance types can all measure the similarity between different time series.

To verify the similarity of two sequence vectors, the recommended criterion is based on the standard deviation of the original time series (Delgado-Bonal & Marshak, 2019; Richman & Moorman, 2000):

$$B_{i,j}^m = \begin{cases} 1 & \text{when} \mathrm{Dis}\left[\Psi_i^m, \Psi_j^m\right] \le r \times \mathrm{std}(H) \\ 0 & \text{when} \mathrm{Dis}\left[\Psi_i^m, \Psi_j^m\right] > r \times \mathrm{std}(H) \text{or} i = j \end{cases} \quad 1 \le i, j \le N - m \tag{4}$$

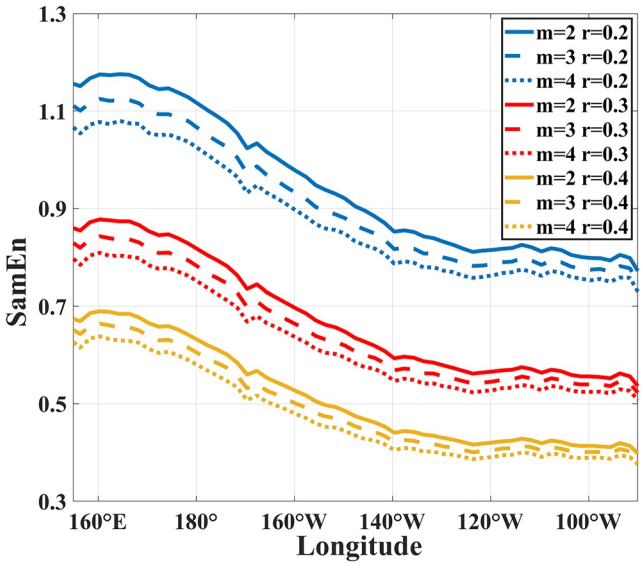

Figure 1. The meridional mean of Sample Entropy value of observed Sea Surface Temperature Anomaly in the tropical Pacific between 10°S and 10°N in the latitude and 155°E and 90°W in the longitude using different parameters ($m = [2, 3, 4]$; $r = [0.2, 0.3, 0.4]$). The temporal range was from 1982 to 2021. The value of m is in days.

where $r \times std(H)$ is a tolerance to determine whether two sequence vectors are similar. Then the numbers of similar vectors in the matrix of sequence vectors are calculated by:

$$B^m = \frac{1}{2}\sum_{i=1}^{N-m}\sum_{j=1}^{N-m} B_{i,j}^m 1 \le i, j \le N - m \tag{5}$$

Next, Ψ^{m+1} is defined as another matrix of sequence vectors of H:

$$\Psi^{m+1} = \begin{bmatrix} H_1 & H_2 & \dots & H_{m+1} \\ H_2 & H_3 & \dots & H_{m+2} \\ \dots & \dots & \dots & \dots \\ H_{N-m} & H_{N-m+1} & \dots & H_N \end{bmatrix} \tag{6}$$

whose number of columns is $m + 1$ and row is $N - m$. The sequence vector of Ψ^{m+1} is defined as one row in Ψ^{m+1}. Similarly, B^{m+1} can be calculated by Ψ^{m+1}.

Finally, SamEn is defined as the proportion of similar numbers between subsequence matrixes Ψ_m and Ψ_{m+1}:

$$\text{SamEn}(m, r) = -ln\left(\frac{B^{m+1}}{B^m}\right) \tag{7}$$

For three-dimensional geophysical variables, such as SSTA (x, y, t) (x represents the longitude, y represents the latitude, and t represents the days), the SamEn of the time series can be calculated in one single grid point, and get the spatial pattern of the SamEn of SSTA.

3. Results and Discussion

3.1. Parameter Determination for SamEn

SamEn is the relative estimation of the sum of positive Lyapunov Exponents (Fraedrich, 1987; Pincus, 1991, 1995; Richman & Moorman, 2000), which can be taken as the degree of the chaos of dynamic systems (Wolff, 1992). The values of SamEn will change with different combinations of parameters for the embedding dimension m and the similarity tolerance r. To determine the parameter combinations of m and r in this study, in Figure 1, the meridional means SamEn values of daily SSTA in the entire tropical Pacific between 1982 and 2021 are investigated using different parameter values to validate the effect of parameters m and r in the calculation of SamEn. The typical values of m and r are between $[2, 4]$ and $[0.2, 0.4]$, respectively, similar to those of the previous studies (Ramdani et al., 2009; Yin et al., 2020; Zhao et al., 2015). The value of m represents the length of sequent vectors of daily SSTA. The change of m does not significantly affect the values of SamEn. The absolute values of SamEn decrease as r increases, while the relative patterns of the SamEn values remain the same. Since only the relative values of SamEn matter, the different combinations of parameters for m and r do not affect our conclusions. Therefore, the SamEn values in this investigation were calculated using $m = 2$ and $r = 0.3$.

3.2. Spatial-Temporal Variation of SamEn

Monthly SamEn values in Niño 3 (5°N–5°S, 150°W–90°W), Niño3.4 (5°N–5°S, 170°E–120°W), and Niño 4 (5°N–5°S, 160°E–150°W) regions are shown in Figure 2. The monthly SamEn values were calculated based on daily SSTA in separate months. For example, when the SamEn value was calculated in January, all the daily data in January between 1982 and 2021 will be used (1,240 data in total). Distinct annual cycles can be observed in all three regions. The SamEn value in the Niño 3 region starts to increase in January, peaks in April with a maximum value of 0.73 and decreases thereafter. The average value equals 0.55. The temporal variation of

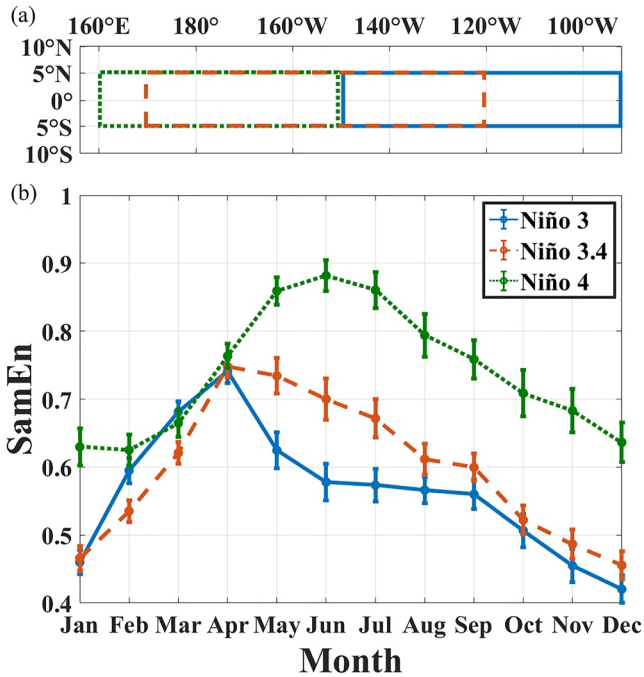

Figure 2. (a) The distributions of Niño 3 region (blue box with solid line), Niño 3.4 region (red box with sparse dash line), and Niño 4 region (green box with dense dash line) in the tropical Pacific. (b) The monthly Sample Entropy values of observed Sea Surface Temperature Anomaly in the Niño 3 region (blue solid line), Niño 3.4 region (red sparse dash line), and Niño 4 region (green dense dash line). Error bars represent the 95% confidence interval.

SamEn in the Niño 3.4 region is comparable to that in Niño 3 with a slightly higher average value of 0.6. The SamEn value in the Niño 4 region starts to increase in February, peaks in June with a maximum value of 0.88 and declines afterward. The average SamEn value in the Niño 4 region reaches 0.75 and is significantly higher than that in other regions, indicating the low predictability of SSTA in the Niño 4 region (Tang et al., 2018). Considering the abovementioned definition of SamEn, the highest degree of chaos exists in spring in the Niño 3 and 3.4 regions and early summer in the Niño 4 region, which are consistent with the known spring PB of SSTA In the Niño 3 and 3.4 regions (Duan & Wei, 2013), and the early summer PB in the Niño 4 region (Hou et al., 2019). Some studies indicated that the Predictability Barrier in Niño 4 region is weak than that in Niño 3 region (Hou et al., 2019; Qi et al., 2021), which is controversial to what was observed in this work. This controversial finding may result from the model deficiencies for simulating the SSTA in Niño 4 region (Lee et al., 2018; Liu et al., 2022; Zheng & Yu., 2017).

Despite the fact that the temporal variation of the PB in the tropical Pacific has been extensively investigated in recent decades (Duan & Wei, 2013; Duan & Wu, 2015), the spatial pattern of PB is less well known (Yu & Kao, 2007). To discuss the chaotic characteristics in the entire tropical Pacific and its connection with PB, the monthly spatial patterns of the SamEn values are shown in Figure 3. It is shown that the SamEn patterns have clear monthly variation over the entire tropical Pacific. In summer, autumn, and winter, the highest SamEn values exist in the western, northwestern, and southwestern tropical Pacific, where the Intertropical Convergence Zone (ITCZ) stripe region and South Pacific Convergence Zone (SPCZ) are defined (Vincent, 1994; Waliser & Gautier, 1993). The complex physical process that includes deep cloud convection, maximum precipitation, and huge atmosphere energy transport in the ITCZ and SPCZ region may lead to the high chaotic characteristic of SSTA in this region (Brown et al., 2020; Schneider et al., 2014). In the central and eastern tropical Pacific between 5°S and 5°N, where ENSO events occur, the SamEn values are significantly lower than in other regions

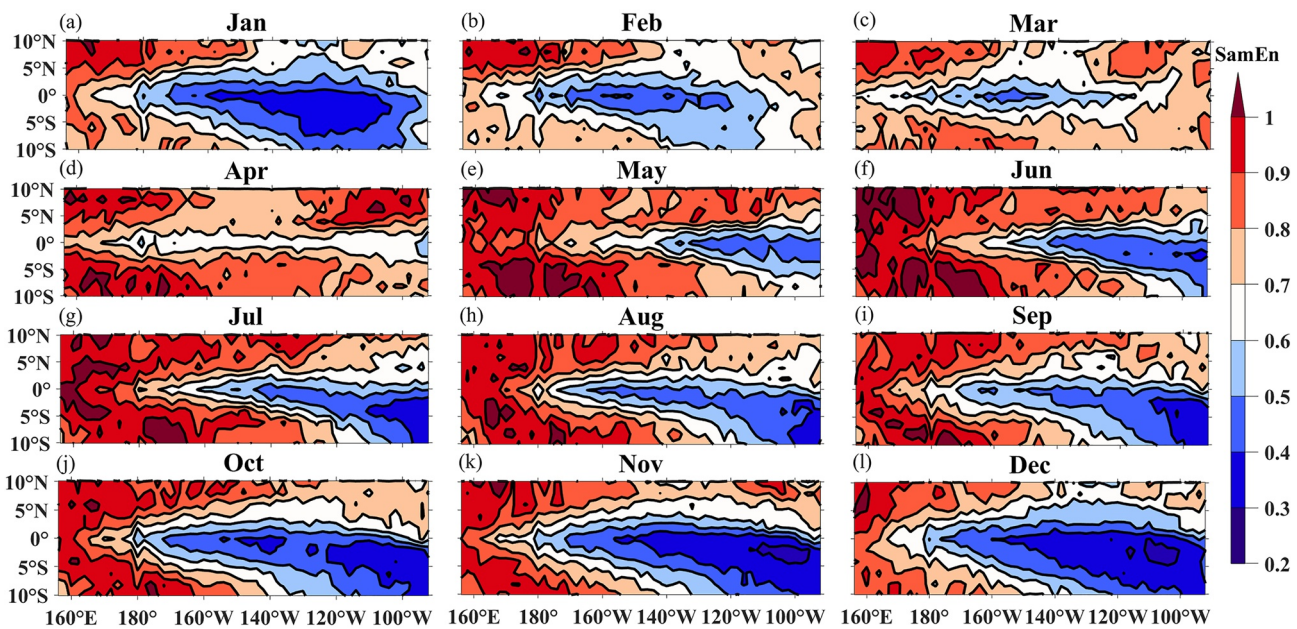

Figure 3. The spatial patterns of Sample Entropy of observed Sea Surface Temperature Anomaly in different months.

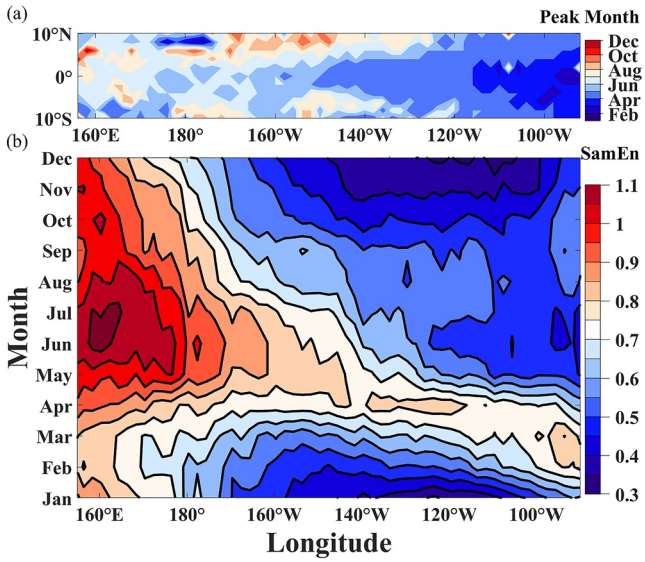

Figure 4. (a) Contour plot of the month when the Sample Entropy has the maximum value, the red number represents the peak month. (b) Contour plot of sample entropy value as a function of longitude and month. The data are averaged between 5°S and 5°N.

in summer, autumn, and winter. The ENSO phenomenon is the most predictable interannual signal in the world (Chen & Cane, 2008; Tang et al., 2018), leading to the low chaotic characteristic of SSTA in these regions. However, in February, March, April, and May, the low SamEn pattern in the eastern tropical Pacific no longer exists. From February, the SamEn values in the eastern tropical Pacific gradually increase, reaching a maximum in April and finally decreasing to the initial state in June. In the central tropical Pacific, the SamEn value reaches its maximum in May, with a lag of 1 to 2 months compared to the variation in the eastern tropical Pacific. The high SamEn patterns appear to originate from the eastern tropical Pacific and propagate westward to increase the SamEn values in the central tropical Pacific.

In Figure 4, the chaotic characteristic of SSTA is investigated as a function of spatial coordinates (i.e., longitude) in the tropical Pacific region using the SamEn method. Figure 4a shows the spatial pattern of the months when the SamEn values peak. The peak months in the eastern tropical Pacific are primarily between March and May; in the central tropical Pacific, it is mainly in May and June; and in the western tropical Pacific, the peak month is after July and exhibits significant spatial variations. The contour plot of the SSTA SamEn values averaged between 5°S and 5°N as a function of longitude coordinates is shown in Figure 4b. From 180°E to 100°W, there is a linear trend of high SamEn values along the longitude may be observed. The month when the SamEn values peak moves from March to June as the coordinates moving westward. Compared with Figure 3, the result further reveals that the chaotic signal might originate in the eastern tropical Pacific during spring, and spread westward linearly to the central tropical Pacific.

To further explore the spatial-temporal features of the SSTA chaotic degree, the variances of monthly SSTA data are shown in Figure 5a. The variances of SSTA are low in the spring (summer) in the eastern (central) tropical Pacific, which displayed a similar spatial-temporal pattern as the one from SamEn in Figure 4b. The variances of SSTA in the tropical Pacific are closely related to the ratio between ENSO (high-amplitude) signal and background (low-amplitude) signal (Torrence & Webster., 1998; Xue et al., 1994). To demonstrate the relation, in Figure 5b, the comparison of the SSTA variances and the ratio between background SSTA signal and ENSO-related signal was shown in Niño 3 region. When the variances of SSTA were large between November and January, the ratios between low-amplitude background signal and high-amplitude ENSO-related signal were low with a minimum value of 0.15, which means the ENSO-related signal was more dominant than the background signal in SSTA during these months. On the contrary, when the variances of SSTA were low between March and May, the ratios between background signals and ENSO-related signals were relatively high, which represented a dominant role of background signals. Hence, the similarity between variations of high SamEn values and low SSTA variances indicated that the low-amplitude background signal was more chaotic than the ENSO-related signal.

3.3. Spatial-Temporal Variation of PB

To investigate the connection between the chaotic background SSTA signals and the PB phenomenon, the forecast errors are examined in the NMME data set, which is defined as the difference between the forecast SSTA value in the NMME data set and the observed SSTA value in the OISST data, starting from January. In Figure 6, the forecast SSTA is the ensemble mean values of the NMME models listed in Table 1. The lead time when forecast errors start to grow rapidly shows a linear variation along the longitude, which is near March and April in the eastern tropical Pacific and June and July in the central tropical Pacific. The spatial-temporal patterns of forecast errors for different forecast models are shown in Figure S2 in Supporting Information S1. Most of the models (except the GFDL-CM2p1-aer04) show similar spatial-temporal variations of forecast errors compared with the results of the ensemble mean in Figure 6. The evolution of forecast errors starting from other months displays similar results (more details can be seen in Figure S3 in Supporting Information S1). The variation of forecasting ability was compatible with the fluctuation of the high SamEn values in Figure 4b and low variances of SSTA data in Figure 5a. When the variances of SSTA data were low, the low-ampliltude chaotic background SSTA

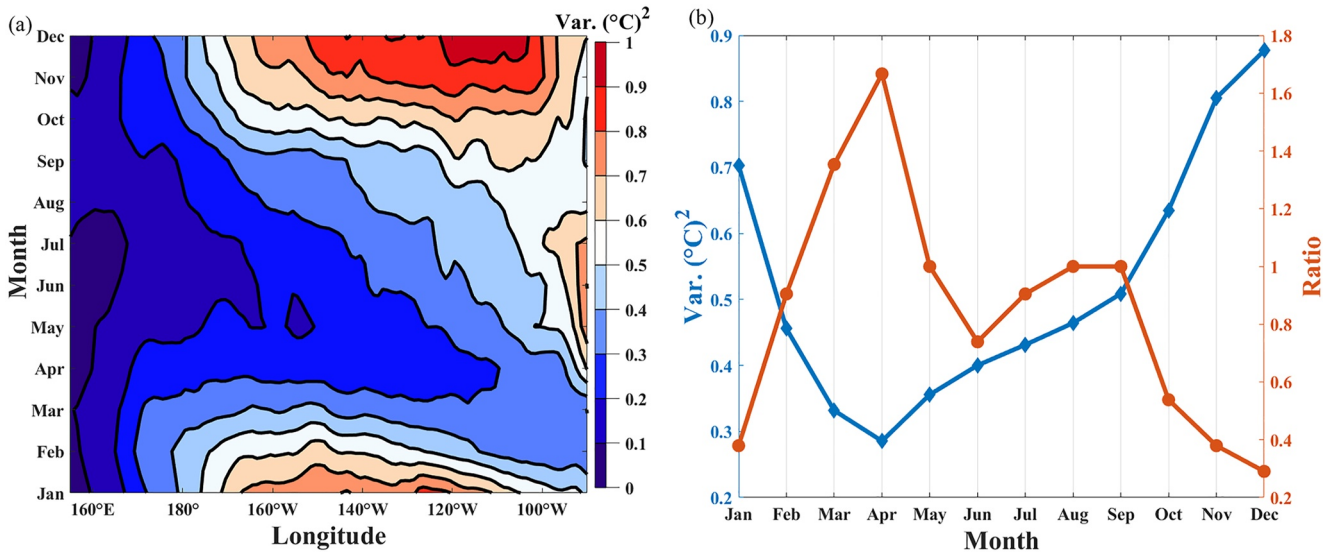

Figure 5. (a) Contour plot of the variances (Var.) of monthly Sea Surface Temperature Anomaly (SSTA) data as a function of longitude and month, the data were averaged between 5°S and 5°N. The color bar represents the monthly variance value of the SSTA. (b) The comparison of the SSTA variances and the ratio between background SSTA signal and El Niño/Southern Oscillation (ENSO)-related signal for different months in the Niño 3 region. The blue line represents the SSTA variances in different months. The SSTA variances values are marked as diamond. The *y*-axis is blue and located on the left. The red line represents the ratio between low-amplitude background SSTA signal and high-amplitude SSTA signal for a different month. The values of the ratio are marked as a solid circle. The *y* axis is red and located on the right. The high-amplitude ENSO-related signal is defined as the average monthly SSTA in Niño 3 region whose values are greater than 0.5°C or less than −0.5°C. The low-amplitude background signal is defined as the average monthly SSTA whose values are greater than −0.5°C and less than 0.5°C. The detailed calculation process of the monthly ratio can be seen in Figure S1 in Supporting Information S1. The monthly SSTA data are from the Optimum Interpolation Sea Surface Temperature data set. The temporal range is from 1982 to 2021.

signal was more dominant than the ENSO-related signal. This chaotic background SSTA signal was inherently difficult to predict as the initial error in the forecast models will grow rapidly, leading to the seasonal PB. Hence, the inherent low predictability of the chaotic background SSTA signal may lead to the seasonal PB of SSTA in the tropical Pacific.

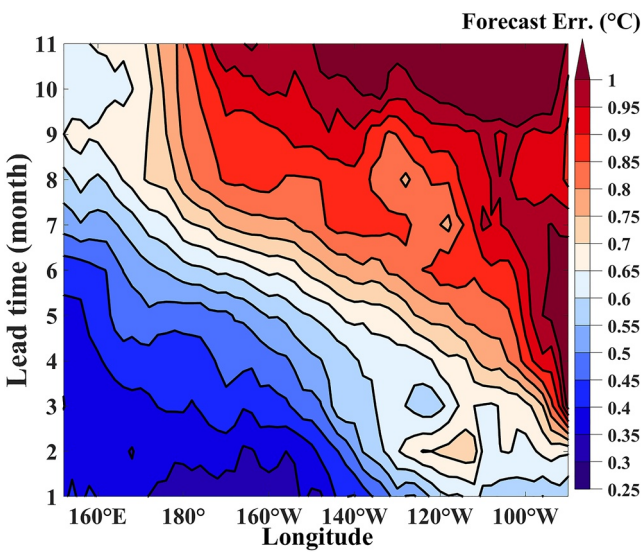

Figure 6. Contour plot of the forecast errors as a function of longitude and lead time, the data are averaged between 5°S and 5°N. The forecast error was calculated by the difference between the observed value in the Optimum Interpolation Sea Surface Temperature data set and the ensemble average of Sea Surface Temperature Anomaly forecast values based on seven NMME models listed in Table 1. The initial month was January. The lead time represented the time after the initial forecast.

3.4. Potential Causes for the Spatial-Temporal Variations of Chaotic Degree

To better understand the potential causes of SSTA chaotic nature, the correlations between the chaotic degree of SSTA and driving forces from the atmosphere and ocean were investigated. In Figure 7, the correlation coefficients of monthly SSTA with the thermocline depth anomaly and shortwave flux anomaly were shown as a function of longitude and month.

In the Niño 3 region, when the chaotic degree was the greatest in the spring, the correlation between SSTA and the thermocline depth anomaly was the weakest, but the correlation with the shortwave flux anomaly was the highest among all seasons. Meanwhile, in the Niño 4 region, when the chaotic degree was the greatest in the summer, the correlation became the least between SSTA and shortwave flux anomaly. The correlation between SSTA and thermocline depth anomaly represents the effect of subsurface thermal state on SSTA variability in the tropical Pacific (Zhu et al., 2015). Hence, the seasonal correlations of SSTA with the ocean subsurface thermal state and the atmospheric forcing may contribute to the high chaotic degree of SSTA in the Niño 3 and Niño 4 regions. Furthermore, the correlation between SSTA and shortwave flux anomalies displayed a similar pattern as one of the SamEn values in Figure 4b, which indicated that the connection between the SSTA and the atmospheric forcing might contribute to the spatial-temporal variations of the

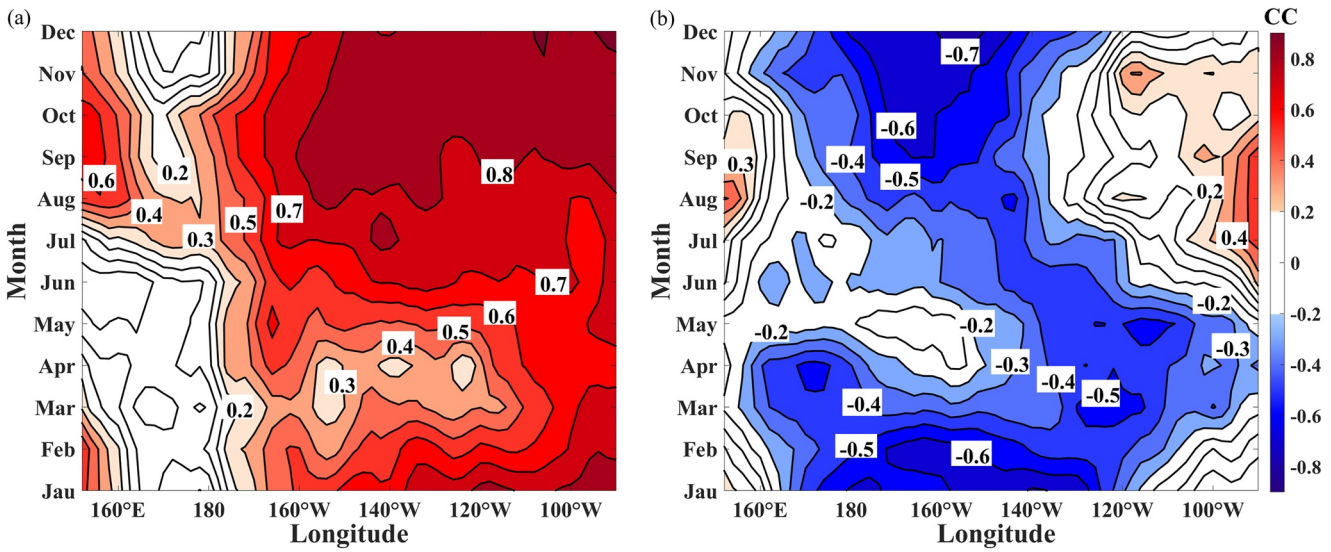

Figure 7. Contour plot of the correlation coefficients between monthly Sea Surface Temperature Anomaly (SSTA) and thermocline depth anomaly (a), and shortwave flux anomaly (b) as a function of longitude and month. The SSTA data and thermocline depth anomaly data are from the HYCOM reanalysis data set. The thermocline depth is defined as the depth of 20°C isotherms in the ocean subsurface. The shortwave flux anomaly data are from the Climate Forecast System Reanalysis and Climate Forecast System Version 2 reanalysis data sets. The temporal range is from 1994 to 2015, which is the maximum range of the HYCOM data set. The spatial-temporal variations of the chaotic degree of HYCOM SSTA were shown in Figure S4 in Supporting Information S1. The westward propagations of high chaotic value are still evident compared with Figure 4b.

chaotic characteristic of SSTA. The correlations between SSTA and other variables related to SSTA variability (e.g., longwave radiations, latent and sensible heat fluxes, surface wind stresses, etc.) did not show consistent spatial-temporal variations compared with that of chaotic degree (not shown here).

4. Conclusions

In this paper, the SamEn method was utilized to identify the nonlinear cause of the seasonal PB of SSTA in the tropical Pacific based on the OISST, the HYCOM, CFSR, and CFSv2 reanalysis data, and the NMME forecast model data sets. The PB phenomenon was found to result from the inherently low predictability of chaotic background SSTA signal. The connection between SSTA and atmospheric forcing may contribute to the spatial-temporal variations of the chaotic signal.

On the monthly scale, the chaotic degree of the observed SSTA peaked in April in Niño 3 and Niño 3.4 regions, May, and June in Niño 4 region, which agreed with the known spring PB in Niño 3 and Niño 3.4 regions and summer PB in Niño 4 region. In these peak months, the air-sea coupled system is more chaotic; in other words, the initial errors will grow faster and finally result in the corresponding seasonal PB of SSTA in these regions.

The monthly spatial patterns of the chaotic degree and its average between 5°S and 5°N along the longitude in the tropical Pacific were investigated. It was revealed that the anomalous high chaotic signal originated in the eastern tropical Pacific in the spring, and then propagated westward to the central tropical Pacific in the summer. The low variance value of SSTA showed a similar westward propagation character along the longitude compared with the chaotic degree. When the variance of SSTA was low, the low background SSTA signal was more dominant than the ENSO-related signal. Hence, the similarity between the variations of high SamEn values and low SSTA variances indicated that the low-amplitude background signal was more chaotic than the ENSO-related signal. Furthermore, the spatial-temporal variations of the PB occurrence timing were similar to that of the high chaotic degree and low variance value of SSTA. Specifically, when the variances of SSTA were low, the chaotic low-amplitude background SSTA signal was dominant, and the PB phenomenon occurred. The chaotic background SSTA signal was inherently difficult to predict as the initial error in the forecast models will grow rapidly, leading to the seasonal PB.

To explore the potential causes for the westward propagation of the SSTA chaotic degree along the longitude in the tropical Pacific, the seasonal correlation coefficients of SSTA with the different variables related to SSTA variability were shown. Only the correlation between SSTA and shortwave flux anomaly showed similar variations along the longitude compared with the chaotic degree, which indicated that the seasonal connection between the SSTA and the atmospheric forcing may contribute to the spatial-temporal variations of the chaotic degree of SSTA.

It should be noted that the PB phenomenon in the tropical Pacific can be represented by a rapid loss of predictability or persistence of the ocean heat content in winter (Balmaseda et al., 1995; McPhaden, 2003; Seleznev & Mukhin, 2022; Yu & Kao, 2007). It is not clear whether the nonlinear cause for the PB of SSTA found in this study is appliable to the PB of the ocean heat content and other physical variables and further studies would be necessary. In addition, there are still some open questions about the physical causes for the spatial-temporal variations of the chaotic degree. For example, in the Niño 3 region, the chaotic degree was high when the atmospheric forcing is more correlated with SSTA in the spring; in the Niño 4 region, the chaotic degree was high when the atmospheric forcing is less correlated with SSTA in the summer. Hence, the atmospheric forcing seems to play a different role in the chaotic nature of SSTA in the Niño 3 and the Niño 4 region. Utilizing the dynamic models may be a better method to investigate the nonlinear characteristic of the system, as the correlation analysis is still based on the linear theory (Bradley & Kantz, 2015). Using a box model for the ENSO phenomenon (Sun, 1997), we have found that the atmospheric forcing directly determines the chaotic behavior of air-sea coupled systems in the tropical Pacific. However, this finding still requires a more rigorous theoretical discussion and is not described in this manuscript. As this work is mainly focused on exploring the nonlinear cause of the Predictability Barrier of SSTA, the detailed role of external forcings in the chaotic nature of SSTA is beyond the scope of this study and will be discussed in future work.

Data Availability Statement

The data used to reproduce the results of this paper are located at https://psl.noaa.gov/data/gridded/data.noaaoisst.v2.highres.html for NOAA Optimum Interpolation Sea Surface Temperature (OISST) V2 High-Resolution Data Set, http://iridl.ldeo.columbia.edu/SOURCES/.Models/.NMME/ for the North American Multi-Model Ensemble (NMME) data set, https://www.hycom.org/dataserver/gofs-3pt1/reanalysis for the HYCOM Global Ocean Forecasting System (GOFS) 3.1 reanalysis data sets, and https://rda.ucar.edu/ for the National Centers for Environmental Prediction (NCEP) Climate Forecast System Reanalysis (CFSR) and Climate Forecast System Version 2 (CFSv2) data.

Acknowledgments
This work is supported by the Sino-Norway Collaborative STRESSOR Project, funded by the Natural Science Foundation of China (NSFC Grant 41861134040) and the Research Council of Norway (RCN Grant 287043). This work is also supported by the Shanghai Frontiers Science Center of Polar Science (SCOPS). We acknowledge the agencies that support the North American Multi-Model Ensemble (NMME) forecast system, and we thank the climate modeling groups (Environment Canada, NASA, NCAR, NOAA/GFDL, NOAA/NCEP, and University of Miami) for producing and making available their model output. We also acknowledge the NOAA PSL, Boulder, Colorado, USA for providing the NOAA OI SST V2 High Resolution Data set data from their website at https://psl.noaa.gov. The authors would like to appreciate the anonymous reviewers for their insightful comments and suggestions to improve this manuscript.

References

Aktaruzzaman, M., & Sassi, R. (2014). Parametric estimation of sample entropy in heart rate variability analysis. *Biomedical Signal Processing and Control*, *14*(1), 141–147. https://doi.org/10.1016/j.bspc.2014.07.011

Balmaseda, M. A., Davey, M. K., & Anderson, D. L. T. (1995). Decadal and seasonal dependence of ENSO prediction skill. *Journal of Climate*, *8*(11), 2705–2715. https://doi.org/10.1175/1520-0442(1995)008<2705:DASDOE>2.0.CO;2

Barnston, A. G., Tippett, M. K., Ranganathan, M., & L'Heureux, M. L. (2019). Deterministic skill of ENSO predictions from the North American multimodel ensemble. *Climate Dynamics*, *53*(12), 7215–7234. https://doi.org/10.1007/s00382-017-3603-3

Becker, E., Kirtman, B. P., & Pegion, K. (2020). Evolution of the North American multi-model ensemble. *Geophysical Research Letters*, *47*(9), 1–9. https://doi.org/10.1029/2020GL087408

Bradley, E., & Kantz, H. (2015). Nonlinear time-series analysis revisited. *Chaos: An Interdisciplinary Journal of Nonlinear Science*, *25*(9), 097610. https://doi.org/10.1063/1.4917289

Brown, J. R., Lengaigne, M., Lintner, B. R., Widlansky, M. J., van der Wiel, K., Dutheil, C., et al. (2020). South Pacific Convergence Zone dynamics, variability and impacts in a changing climate. *Nature Reviews Earth & Environment*, *1*(10), 530–543. https://doi.org/10.1038/s43017-020-0078-2

Castro, C. L., McKee, T. B., & Pielke, R. A. (2001). The relationship of the North American Monsoon to tropical and North Pacific Sea surface temperatures as revealed by observational analyses. *Journal of Climate*, *14*(24), 4449–4473. https://doi.org/10.1175/15200442(2001)014<4449:TROTNA>2.0.CO;2

Chassignet, E. P., Hurlburt, H. E., Smedstad, O. M., Halliwell, G. R., Hogan, P. J., Wallcraft, A. J., et al. (2007). The HYCOM (HYbrid Coordinate Ocean Model) data assimilative system. *Journal of Marine Systems*, *65*(1–4), 60–83. https://doi.org/10.1016/j.jmarsys.2005.09.016

Chen, D., & Cane, M. A. (2008). El Niño prediction and predictability. *Journal of Computational Physics*, *227*(7), 3625–3640. https://doi.org/10.1016/j.jcp.2007.05.014

Chong-Yin, L., & Jian, L. (2009). Physical essence of the "predictability barrier. *Atmospheric and Oceanic Science Letters*, *2*(5), 290–294. https://doi.org/10.1080/16742834.2009.11446810

Clancy, R., Bitz, C., & Blanchard-Wrigglesworth, E. (2021). The influence of ENSO on Arctic sea ice in large ensembles and observations. *Journal of Climate*, 1–50. https://doi.org/10.1175/jcli-d-20-0958.1

Collins, M., Frame, D., Sinha, B., & Wilson, C. (2002). How far ahead could we predict El Niño? *Geophysical Research Letters*, *29*(10), 130–134. https://doi.org/10.1029/2001GL013919

Dash, M. K., Pandey, P. C., Vyas, N. K., & Turner, J. (2013). Variability in the ENSO-induced southern hemispheric circulation and Antarctic sea ice extent. *International Journal of Climatology*, *33*(3), 778–783. https://doi.org/10.1002/joc.3456

Delgado-Bonal, A., & Marshak, A. (2019). Approximate entropy and sample entropy: A comprehensive tutorial. *Entropy*, *21*(6), 1–37. https://doi.org/10.3390/e21060541

Duan, W., & Wei, C. (2013). The "spring predictability barrier" for ENSO predictions and its possible mechanism: Results from a fully coupled model. *International Journal of Climatology*, *33*(5), 1280–1292. https://doi.org/10.1002/joc.3513

Duan, W., & Wu, Y. (2015). Season-dependent predictability and error growth dynamics of Pacific Decadal Oscillation-related sea surface temperature anomalies. *Climate Dynamics*, *44*(3–4), 1053–1072. https://doi.org/10.1007/s00382-014-2364-5

Eduardo Virgilio Silva, L., & Otavio Murta, L. (2012). Evaluation of physiologic complexity in time series using generalized sample entropy and surrogate data analysis. *Chaos: An Interdisciplinary Journal of Nonlinear Science*, *22*(4), 043105. https://doi.org/10.1063/1.4758815

Fereday, D. R., Knight, J. R., Scaife, A. A., Folland, C. K., & Philipp, A. (2008). Cluster analysis of North Atlantic-European circulation types and links with tropical Pacific Sea surface temperatures. *Journal of Climate*, *21*(15), 3687–3703. https://doi.org/10.1175/2007JCLI1875.1

Fraedrich, K. (1987). Estimating weather and climate predictability on attractors. *Journal of the Atmospheric Sciences*, *44*(4), 722–728. https://doi.org/10.1175/15200469(1987)044<0722:EWACPO>2.0.CO;2

Gao, H., Wang, Y., & He, J. (2006). Weakening significance of ENSO as a predictor of summer precipitation in China. *Geophysical Research Letters*, *33*(9), L09807. https://doi.org/10.1029/2005GL025511

Hou, M., Duan, W., & Zhi, X. (2019). Season-dependent predictability barrier for two types of El Niño revealed by an approach to data analysis for predictability. *Climate Dynamics*, *53*(9–10), 5561–5581. https://doi.org/10.1007/s00382-019-04888-w

Hu, Q., & Feng, S. (2012). AMO- and ENSO-driven summertime circulation and precipitation variations in North America. *Journal of Climate*, *25*(19), 6477–6495. https://doi.org/10.1175/JCLI-D-11-00520.1

Hu, S., Fedorov, A. V., Lengaigne, M., & Guilyardi, E. (2014). The impact of westerly wind bursts on the diversity and predictability of El Niño events: An ocean energetics perspective. *Geophysical Research Letters*, *41*(13), 4654–4663. https://doi.org/10.1002/2014GL059573

Hua, L., Sun, D. Z., & Yu, Y. (2019). Why do we have El Niño: Quantifying a diabatic and nonlinear perspective using observations. *Climate Dynamics*, *52*(11), 6705–6717. https://doi.org/10.1007/s00382-018-4541-4

Huang, B., Liu, C., Banzon, V., Freeman, E., Graham, G., Hankins, B., et al. (2021). Improvements of the Daily Optimum Interpolation Sea surface temperature (DOISST) version 2.1. *Journal of Climate*, *34*(8), 2923–2939. https://doi.org/10.1175/JCLI-D-20-0166.1

Infanti, J. M., & Kirtman, B. P. (2016). North American rainfall and temperature prediction response to the diversity of ENSO. *Climate Dynamics*, *46*(9–10), 3007–3023. https://doi.org/10.1007/s00382-015-2749-0

Jin, E. K., Kinter, J. L., Wang, B., Park, C. K., Kang, I. S., Kirtman, B. P., et al. (2008). Current status of ENSO prediction skill in coupled ocean-atmosphere models. *Climate Dynamics*, *31*(6), 647–664. https://doi.org/10.1007/s00382-008-0397-3

Jin, Y., Liu, Z., & Duan, W. (2022). The Different Relationships between the ENSO Spring Persistence Barrier and Predictability Barrier. *Journal of Climate*, *35*(18), 6207–6218. https://doi.org/10.1175/jcli-d-22-0013.1

Kantz, H., & Schreiber, T. (2003). *Nonlinear time series analysis*. Cambridge University Press. https://doi.org/10.1017/CBO9780511755798

Karamperidou, C., Cane, M. A., Lall, U., & Wittenberg, A. T. (2014). Intrinsic modulation of ENSO predictability viewed through a local Lyapunov lens. *Climate Dynamics*, *42*(1–2), 253–270. https://doi.org/10.1007/s00382-013-1759-z

Kim, I. (2021). Multiscale sample entropy of two-dimensional decaying turbulence. *Entropy*, *23*(2), 1–9. https://doi.org/10.3390/e23020245

Kirtman, B. P., & Min, D. (2009). Multimodel ensemble ENSO prediction with CCSM and CFS. *Monthly Weather Review*, *137*(9), 2908–2930. https://doi.org/10.1175/2009MWR2672.1

Kirtman, B. P., Min, D., Infanti, J. M., Kinter, J. L., Paolino, D. A., Zhang, Q., et al. (2014). The North American multimodel ensemble: Phase-1 seasonal-to-interannual prediction; phase-2 toward developing intraseasonal prediction. *Bulletin of the American Meteorological Society*, *95*(4), 585–601. https://doi.org/10.1175/BAMS-D-12-00050.1

Kløve, T. (2011). Lower bounds on the size of spheres of permutations under the Chebychev distance. *Designs, Codes and Cryptography*, *59*(1–3), 183–191. https://doi.org/10.1007/s10623-010-9454-0

Lake, D. E., Richman, J. S., Pamela Griffin, M., & Randall Moorman, J. (2002). Sample entropy analysis of neonatal heart rate variability. *American Journal of Physiology - Regulatory, Integrative and Comparative Physiology*, *283*(3 52–3), 789–797. https://doi.org/10.1152/ajpregu.00069.2002

Larson, S. M., & Kirtman, B. P. (2015). An alternate approach to ensemble ENSO forecast spread: Application to the 2014 forecast. *Geophysical Research Letters*, *42*(21), 9411–9415. https://doi.org/10.1002/2015GL066173

Latora, V., & Baranger, M. (1999). Kolmogorov-sinai entropy rate versus physical entropy. *Physical Review Letters*, *82*(3), 520–523. https://doi.org/10.1103/PhysRevLett.82.520

Lau, K. M., & Yang, S. (1996). The Asian monsoon and predictability of the tropical ocean-atmosphere system. *Quarterly Journal of the Royal Meteorological Society*, *122*(532), 945–957. https://doi.org/10.1256/smsqj.53207

Lee, R. W. K., Tam, C. Y., Sohn, S. J., & Ahn, J. B. (2018). Predictability of two types of El Niño and their climate impacts in boreal spring to summer in coupled models. *Climate Dynamics*, *51*(11–12), 4555–4571. https://doi.org/10.1007/s00382-017-4039-5

Levine, A. F. Z., & McPhaden, M. J. (2015). The annual cycle in ENSO growth rate as a cause of the spring predictability barrier. *Geophysical Research Letters*, *42*(12), 5034–5041. https://doi.org/10.1002/2015GL064309

Li, J., & Ding, R. (2013). Temporal-spatial distribution of the predictability limit of monthly sea surface temperature in the global oceans. *International Journal of Climatology*, *33*(8), 1936–1947. https://doi.org/10.1002/joc.3562

Liang, J., Yang, X. Q., & Sun, D. Z. (2012). The effect of ENSO events on the tropical Pacific mean climate: Insights from an analytical model. *Journal of Climate*, *25*(21), 7590–7606. https://doi.org/10.1175/JCLI-D-11-00490.1

Liang, J., Yang, X. Q., & Sun, D. Z. (2017). Factors determining the asymmetry of ENSO. *Journal of Climate*, *30*(16), 6097–6106. https://doi.org/10.1175/JCLI-D-16-0923.1

Lin, H., Merryfield, W. J., Muncaster, R., Smith, G. C., Markovic, M., Dupont, F., et al. (2020). The Canadian seasonal to interannual prediction system version 2 (CanSIPSv2). *Weather and Forecasting*, *35*(4), 1317–1343. https://doi.org/10.1175/WAF-D-19-0259.1

Liu, D., Duan, W., Feng, R., & Tang, Y. (2018). Summer predictability barrier of Indian Ocean Dipole events and corresponding error growth dynamics. *Journal of Geophysical Research: Oceans*, *123*(5), 3635–3650. https://doi.org/10.1029/2017JC013739

Liu, T., Song, X., & Tang, Y. (2022). The predictability study of the two flavors of ENSO in the CESM model from 1881 to 2017. *Climate Dynamics*, 1–16. https://doi.org/10.1007/s00382-022-06269-2

Lopez, H., & Kirtman, B. P. (2014). WWBs, ENSO predictability, the spring barrier and extreme events. *Journal of Geophysical Research*, *119*(17), 10114–10138. https://doi.org/10.1002/2014JD021908

Lorenz, E. N. (1963). Deterministic nonperiodic flow. *Journal of the Atmospheric Sciences*, *20*(2), 130–141. https://doi.org/10.1175/1520-0469(1963)020<0130:dnf>2.0.co;2

Marzban, C., & Schaefer, J. T. (2001). The correlation between U.S. tornadoes and Pacific sea surface temperatures. *Monthly Weather Review*, *129*(4), 884–895. https://doi.org/10.1175/1520-0493(2001)129<0884:TCBUST>2.0.CO;2

Mayer, C. C., Bachler, M., Hörtenhuber, M., Stocker, C., Holzinger, A., & Wassertheurer, S. (2014). Selection of entropy-measure parameters for knowledge discovery in heart rate variability data. *BMC Bioinformatics*, *15*(6), 1–11. https://doi.org/10.1186/1471-2105-15-S6-S2

McKinnon, K. A., Rhines, A., Tingley, M. P., & Huybers, P. (2016). Long-lead predictions of eastern United States hot days from Pacific sea surface temperatures. *Nature Geoscience*, *9*(5), 389–394. https://doi.org/10.1038/ngeo2687

McPhaden, M. J. (2003). Tropical Pacific Ocean heat content variations and ENSO persistence barriers. *Geophysical Research Letters*, *30*(9), 1480. https://doi.org/10.1029/2003GL016872

Moore, A. M. (1999). The dynamics of error growth and predictability in a model of the Gulf Stream. Part II: Ensemble prediction. *Journal of Physical Oceanography*, *29*(4), 762–778. https://doi.org/10.1175/1520-0485(1999)029<0762:TDOEGA>2.0.CO;2

Mukhin, D., Gavrilov, A., Seleznev, A., & Buyanova, M. (2021). An atmospheric signal lowering the spring predictability barrier in statistical ENSO forecasts. *Geophysical Research Letters*, *48*(6), 1–10. https://doi.org/10.1029/2020GL091287

Patt, A., & Gwata, C. (2002). Effective seasonal climate forecast applications: Examining constraints for subsistence farmers in Zimbabwe. *Global Environmental Change*, *12*(3), 185–195. https://doi.org/10.1016/S0959-3780(02)00013-4

Pierce, W. D. W. (2002). The role of sea surface temperatures in interactions between ENSO and the North Pacific Oscillation. *Journal of Climate*, *15*(11), 1295–1308. https://doi.org/10.1175/1520-0442(2002)015<1295:trosst>2.0.co;2

Pincus, S. (1995). Approximate entropy (ApEn) as a complexity measure. *Chaos: An Interdisciplinary Journal of Nonlinear Science*, *5*(1), 110–117. https://doi.org/10.1063/1.166092

Pincus, S. M. (1991). Approximate entropy as a measure of system complexity. *Proceedings of the National Academy of Sciences*, *88*(6), 2297–2301. https://doi.org/10.1073/pnas.88.6.2297

Qi, Q., Duan, W., & Xu, H. (2021). The most sensitive initial error modes modulating intensities of CP- and EP- El Niño events. *Dynamics of Atmospheres and Oceans*, *96*, 101257. https://doi.org/10.1016/j.dynatmoce.2021.101257

Ramdani, S., Seigle, B., Lagarde, J., Bouchara, F., & Bernard, P. L. (2009). On the use of sample entropy to analyze human postural sway data. *Medical Engineering & Physics*, *31*(8), 1023–1031. https://doi.org/10.1016/j.medengphy.2009.06.004

Ren, H. L., Jin, F. F., Tian, B., & Scaife, A. A. (2016). Distinct persistence barriers in two types of ENSO. *Geophysical Research Letters*, *43*(20), 10973–10979. https://doi.org/10.1002/2016GL071015

Richman, J. S., & Moorman, J. R. (2000). Physiological time-series analysis using approximate entropy and sample entropy maturity in premature infants Physiological time-series analysis using approximate entropy and sample entropy. *Americal Journal of Physiology Heart and Circulatory Physiology*, *278*(6), H2039–H2049. https://doi.org/10.1152/ajpheart.2000.278.6.h2039

Ropelewski, C. F., & Halpert, M. S. (1986). North American precipitation and temperature patterns associated with the El Nino/Southern Oscillation (ENSO). *Monthly Weather Review*, *114*(12), 2352–2362. https://doi.org/10.1175/1520-0493(1986)114<2352:NAPATP>2.0.CO;2

Samelson, R. M., & Tziperman, E. (2001). Instability of the chaotic ENSO: The growth-phase predictability barrier. *Journal of the Atmospheric Sciences*, *58*(23), 3613–3625. https://doi.org/10.1175/1520-0469(2001)058<3613:IOTCET>2.0.CO;2

Schneider, T., Bischoff, T., & Haug, G. H. (2014). Migrations and dynamics of the intertropical convergence zone. *Nature*, *513*(7516), 45–53. https://doi.org/10.1038/nature13636

Seleznev, A., & Mukhin, D. (2022). Improving statistical prediction and revealing nonlinearity of ENSO using observations of ocean heat content in the tropical Pacific. *Climate Dynamics*. https://doi.org/10.1007/s00382-022-06298-x

Shi, W., & Shang, P. (2013). Cross-sample entropy statistic as a measure of synchronism and cross-correlation of stock markets. *Nonlinear Dynamics*, *71*(3), 539–554. https://doi.org/10.1007/s11071-012-0680-z

Solow, A. R., Adams, R. F., Bryant, K. J., Legler, D. M., O'Brien, J. J., McCarl, B. A., et al. (1998). The value of improved ENSO prediction to U.S. Agriculture. *Climatic Change*, *39*(1), 47–60. https://doi.org/10.1023/A:1005342500057

Song, Y., Zhao, Y., Yin, X., Bao, Y., & Qiao, F. (2020). Evaluation of FIO-ESM v1.0 seasonal prediction skills over the North Pacific. *Frontiers in Marine Science*, *7*, 504. https://doi.org/10.3389/fmars.2020.00504

Sun, D.-Z. (1997). El Niño: A coupled response to radiative heating? *Geophysical Research Letters*, *24*(16), 2031–2034. https://doi.org/10.1029/97GL01960

Tang, Y., Zhang, R.-H., Liu, T., Duan, W., Yang, D., Zheng, F., et al. (2018). Progress in ENSO prediction and predictability study. *National Science Review*, *5*(6), 826–839. https://doi.org/10.1093/nsr/nwy105

Thelier, J. (1987). Efficient algorithm for estimating the correlation dimension from a set of discrete points. *Physical Review A*, *36*(9), 4456–4462. https://doi.org/10.1103/physreva.36.4456

Torrence, C., & Webster, P. J. (1998). The annual cycle of persistence in the El Nino/Southern Oscillation. *Quarterly Journal of the Royal Meteorological Society*, *124*(550), 1985–2004. https://doi.org/10.1256/smsqj.55009

Trenberth, K. E., Branstator, G. W., Karoly, D., Kumar, A., Lau, N. C., & Ropelewski, C. (1998). Progress during TOGA in understanding and modeling global teleconnections associated with tropical sea surface temperatures. *Journal of Geophysical Research*, *103*(C7), 14291–14324. https://doi.org/10.1029/97jc01444

van Oldenborgh, G. J., Balmaseda, M. A., Ferranti, L., Stockdale, T. N., & Anderson, D. L. T. (2005). Did the ECMWF seasonal forecast model outperform statistical ENSO forecast models over the last 15 years? *Journal of Climate*, *18*(16), 3240–3249. https://doi.org/10.1175/JCLI3420.1

Vincent, D. G. (1994). The South Pacific Convergence Zone (SPCZ): A review. *Monthly Weather Review*, *122*(9), 1949–1970. https://doi.org/10.1175/1520-0493(1994)122<1949:TSPCZA>2.0.CO;2

Waliser, D. E., & Gautier, C. (1993). A satellite-derived climatology of the ITCZ. *Journal of Climate*, *6*(11), 2162–2174. https://doi.org/10.1175/15200442(1993)006<2162:ASDCOT>2.0.CO;2

Wang, D., Singh, V. P., Shang, X., Ding, H., Wu, J., Wang, L., et al. (2014). Sample entropy-based adaptive wavelet de-noising approach for meteorologic and hydrologic time series. *Journal of Geophysical Research*, *119*(14), 8726–8740. https://doi.org/10.1002/2014JD021869

Wang, H., & Ting, M. (2000). Covariabilities of winter U.S. precipitation and Pacific Sea surface temperatures. *Journal of Climate*, *13*(20), 3711–3719. https://doi.org/10.1175/1520-0442(2000)013<3711:COWUSP>2.0.CO;2

Webster, P. J. (1995). The annual cycle and the predictability of the tropical coupled ocean-atmosphere system. *Meteorology and Atmospheric Physics*, *56*(1–2), 33–55. https://doi.org/10.1007/BF01022520

Webster, P. J., & Yang, S. (1992). Monsoon and enso: Selectively interactive systems. *Quarterly Journal of the Royal Meteorological Society*, *118*(507), 877–926. https://doi.org/10.1002/qj.49711850705

Wolf, A., Swift, J. B., Swinney, H. L., & Vastano, J. A. (1985). Determining Lyapunov exponents from a time series. *Physica D: Nonlinear Phenomena*, *16*(3), 285–317. https://doi.org/10.1016/0167-2789(85)90011-9

Wolff, R. C. L. (1992). Local Lyapunov exponents: Looking closely at chaos. *Journal of the Royal Statistical Society: Series B*, *54*(2), 353–371. https://doi.org/10.1111/j.2517-6161.1992.tb01886.x

Wu, R., Hu, Z. Z., & Kirtman, B. P. (2003). Evolution of ENSO-related rainfall anomalies in East Asia. *Journal of Climate*, *16*(22), 3742–3758. https://doi.org/10.1175/1520-0442(2003)016<3742:EOERAI>2.0.CO;2

Xue, Y., Cane, M. A., Zebiak, S. E., & Blumenthal, M. B. (1994). On the prediction of ENSO: A study with a low-order Markov model. *Tellus*, *46*(4), 512–528. https://doi.org/10.1034/j.1600-0870.1994.00013.x

Xue, Y., Chen, M., Kumar, A., Hu, Z. Z., & Wang, W. (2013). Prediction skill and bias of tropical Pacific sea surface temperatures in the NCEP climate forecast system version 2. *Journal of Climate*, *26*(15), 5358–5378. https://doi.org/10.1175/JCLI-D-12-00600.1

Yentes, J. M., Hunt, N., Schmid, K. K., Kaipust, J. P., McGrath, D., & Stergiou, N. (2013). The appropriate use of approximate entropy and sample entropy with short data sets. *Annals of Biomedical Engineering*, *41*(2), 349–365. https://doi.org/10.1007/s10439-012-0668-3

Yin, J., Xiao, P. X., Li, J., Liu, Y., Yan, C., & Zhang, Y. (2020). Parameters analysis of sample entropy, permutation entropy and permutation ratio entropy for RR interval time series. *Information Processing & Management*, *57*(5), 102283. https://doi.org/10.1016/j.ipm.2020.102283

Yu, J. Y., & Kao, H. Y. (2007). Decadal changes of ENSO persistence barrier in SST and ocean heat content indices: 1958-2001. *Journal of Geophysical Research*, *112*(13), 1–10. https://doi.org/10.1029/2006JD007654

Yuan, X. (2004). ENSO-related impacts on Antarctic sea ice: A synthesis of phenomenon and mechanisms. *Antarctic Science*, *16*(4), 415–425. https://doi.org/10.1017/S0954102004002238

Yuan, Y., & Yang, S. (2012). Impacts of different types of El NiñO on the East Asian climate: Focus on ENSO cycles. *Journal of Climate*, *25*(21), 7702–7722. https://doi.org/10.1175/JCLI-D-11-00576.1

Zhang, L., Li, H., Liu, D., Fu, Q., Li, M., Faiz, M. A., et al. (2019). Identification and application of the most suitable entropy model for precipitation complexity measurement. *Atmospheric Research*, *221*, 88–97. https://doi.org/10.1016/j.atmosres.2019.02.002

Zhao, L., Wei, S., Zhang, C., Zhang, Y., Jiang, X., Liu, F., & Liu, C. (2015). Determination of sample entropy and fuzzy measure entropy parameters for distinguishing congestive heart failure from normal sinus rhythm subjects. *Entropy*, *17*(9), 6270–6288. https://doi.org/10.3390/e17096270

Zheng, F., & Yu, J. Y. (2017). Contrasting the skills and biases of deterministic predictions for the two types of El Niño. *Advances in Atmospheric Sciences*, *34*(12), 1395–1403. https://doi.org/10.1007/s00376-017-6324-y

Zheng, F., & Zhu, J. (2010). Spring predictability barrier of ENSO events from the perspective of an ensemble prediction system. *Global and Planetary Change*, *72*(3), 108–117. https://doi.org/10.1016/j.gloplacha.2010.01.021

Zhu, J., Kumar, A., & Huang, B. (2015). The relationship between thermocline depth and SST anomalies in the eastern equatorial Pacific: Seasonality and decadal variations. *Geophysical Research Letters*, *42*(11), 4507–4515. https://doi.org/10.1002/2015GL064220